Nitrogen Doping Effects on Carbon Nanotubes and the Origin of the Enhanced Electrocatalytic Activity of Supported Pt for Proton-Exchange Membrane Fuel Cells

Yougui Chen,[†] Jiajun Wang,[†] Hao Liu,[†] Mohammad Norouzi Banis,[†] Ruying Li,[†] Xueliang Sun,*,[†] Tsun-Kong Sham,[‡] Siyu Ye,[§] and Shanna Knights[§]

[†]Department of Mechanical and Materials Engineering, University of Western Ontario, London, Ontario, Canada N6A 5B9

[‡]Department of Chemistry, University of Western Ontario, London, Ontario, Canada N6A 5B7

[§]Ballard Power Systems Inc., 9000 Glenlyon Parkway, Burnaby, BC, Canada V5J 5J8

Ⓢ *Supporting Information*

ABSTRACT: Carbon nanotubes (CNTs) and nitrogen-doped carbon nanotubes (CNx) were synthesized by the floating catalyst chemical vapor deposition (FCCVD) method. Pt nanoparticles were deposited onto the two catalyst supports with the ethylene glycol reduction method. Different from CNTs that contain straight hollow tubes, CNx contain a bamboolike structure with kinks along the tubes and more surface defects. X-ray photoelectron spectroscopy (XPS) confirms the nitrogen atoms in the graphite matrix and reveals the chemical natures of the doped nitrogen atoms. Carbon K-edge near-edge X-ray absorption fine structure (NEXAFS) and Raman characterizations reveal higher defectiveness in CNx than CNTs. The unique

structure and surface property of CNx leads to a better dispersion of Pt nanoparticles on CNx than on CNTs, as revealed by TEM images. Pt supported on CNx (Pt/CNx) exhibited a higher electrochemical surface area (ECSA) and higher catalytic activity toward oxygen reduction reaction (ORR), in comparison to Pt supported on CNTs (Pt/CNTs). Better performance of Pt/CNx than Pt/CNTs has been confirmed by single-cell fuel cell tests.
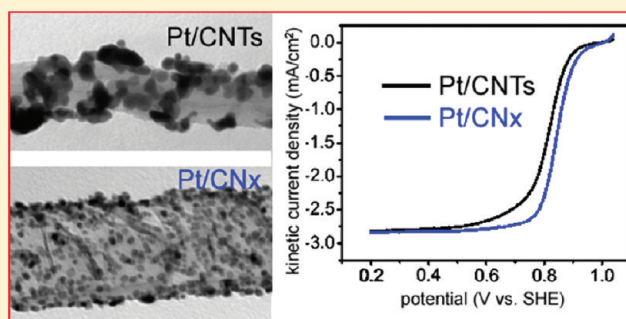
1. INTRODUCTION

Because of the depletion of fossil fuels and rising environmental pollutions, fuel cells have attracted attention from governments and industries as an important clean energy alternative in the future. Among various fuel cells, proton-exchange membrane fuel cell (PEMFC) is the most developed in the past two decades, featuring rapid start-up and high power density, making it suitable for many applications including stationary and automotive applications.[1] Despite these advantages, low durability[2] and high cost[3] still hamper its widespread commercialization. It is well-known that all these disadvantages are directly related to the catalysts used in PEMFC to catalyze oxygen reduction (ORR) and hydrogen oxidation reactions.

Until now, the state-of-the-art catalyst involves Pt nanoparticles supported on carbon black (e.g., Vulcan XC 72). As a catalyst support, in spite of its high surface area and good electrochemical performance, carbon black is still unsatisfactory. Because of the weak interaction between Pt and carbon black, Pt nanoparticles aggregate into larger particles or dissolve into the polymer electrolyte, which results in a decrease in Pt surface area and fuel cell performance.[4] Furthermore, Pt nanoparticles deposited within the porous carbon nanostructure may be inaccessible to the

polymer electrolyte and hence reduce the utilization of Pt.[5] In addition, carbon black suffers from corrosion (to form surface oxides and/or even CO and CO_2 evolution) at the cathode of the PEMFC,[6−8] where there is high potential, moisture, and perhaps hydrogen peroxide. Therefore, a tremendous effort is being devoted to the development of better catalyst support materials.

Recently, novel carbon nanostructure materials such as carbon nanotubes (CNTs) have attracted great attention as promising catalyst supports. The smooth graphitic surface could make all Pt nanoparticles on CNTs accessible to the reactants. The high surface area of CNTs with their unique nanostructure could lead to a high dispersion of Pt nanoparticles. Additionally, due to the graphitic structure, CNTs maintain high electrical conductivity and corrosion resistance; both of which are critical for an excellent catalyst support. It has been shown that CNTs are better catalyst supports than conventional carbon black. CNTs exhibit higher electrochemical corrosion resistance than carbon black.[9,10] Furthermore, Pt supported on CNTs (Pt/CNTs) also show a higher

electrocatalytic activity[11−15] and stability[10,16] than Pt/C. In spite of these advantages, the uniform dispersion of Pt nanoparticles onto CNTs still remains a formidable challenge because of the inert surface of CNTs. Therefore, harsh chemical or electrochemical oxidations applied with concentrated strong acid are typically employed to create oxygen-containing surface functionalities, which facilitate the attachment of Pt nanoparticles.[17] However, these severe treatments also significantly deteriorate the preferred structure and electrical properties of CNTs due to the destruction of the graphitic structure.[18]

Alternatively, doping with foreign atoms (e.g., nitrogen) represents a feasible path to increase reactivity toward the deposition of metal nanoparticles. The doping of nitrogen in CNTs creates defects that break out the chemical inertness of pure CNTs, yet preserves the electrical conductivity. Nitrogen-doped carbon nanotubes (CNx) contain nitrogenated sites that are chemically active. Therefore, it should be possible to avoid those detrimental functionalization processes using strong acid and to attach Pt nanoparticles onto the surface of CNx effectively. In addition, nitrogen-doped carbon itself has a certain activity toward ORR.[19,20] Recently, CNx have been reported as support materials in fuel cell catalysts.[21−24] Our preliminary work indicates that CNx works better as catalyst supports than CNTs in PEMFC in terms of better Pt dispersion and thus higher fuel cell performance.[21] Besides the superior performance, Pt supported on CNx (Pt/CNx) has been shown to exhibit a higher durability both by theoretical calculations[25,26] and by our experimental work.[27]

Because the sluggish kinetics of the ORR has been a major bottleneck in the performance of PEMFCs, the current work focuses on the cathode. We have reported a preliminary study on Pt nanoparticles deposited on a CNx/carbon paper composite electrode of an enhanced activity compared with CNTs/carbon paper.[21] Here, systematic experiments were conducted to investigate the nitrogen doping effects on CNTs and the enhanced electrocatalytic activity of powder Pt/CNx catalysts. A comprehensive understanding of the nitrogen doping effects on CNTs and the origin of enhanced activity of the deposited Pt emerges.

2. EXPERIMENTAL SECTION

2.1. Synthesis of CNTs and CNx. CNTs and CNx were grown directly on carbon paper via the floating catalyst chemical vapor deposition (FCCVD) method in a horizontal quartz tube furnace system, as described before in detail.[28] In short, a carbon paper with a 30 nm Al buffer layer was applied as the substrate. Ethylene and ferrocene were used as the carbon source and catalyst precursor, respectively. CNTs were synthesized at 850 °C with a gas flow of ethylene (10 sccm) and Ar (500 sccm). Ferrocene decomposed into iron, which deposited onto the carbon paper and acted as the catalyst for CNTs growth. Two grams of melamine was employed as the nitrogen precursor for the synthesis of CNx. At 950 °C, melamine decomposed into nitrogen atoms, which were incorporated into the graphite structure during the growth of CNTs to yield CNx.

2.2. Pt Deposition. Pt nanoparticles were deposited on the pristine CNTs (or CNx) by the ethylene glycol reduction method at a Pt metal loading of 30 wt %.[29] Typically, 15 mg of CNTs (or CNx) were dispersed in ethylene glycol with ultrasonication. Then 17.1 mg of $H_2PtCl_6 \cdot 6H_2O$ was added into the suspension. After refluxing at 160 °C for 3 h, the suspension was cooled down to room temperature naturally. The catalysts were

collected with filtration and washed with ample deionized water. The colorless and transparent filtrate indicated that all of the $H_2PtCl_6 \cdot 6H_2O$ was reduced into Pt metal and deposited on CNTs (or CNx). The Pt/CNTs (or Pt/CNx) thus obtained was dried at 60 °C overnight.

2.3. Physical Characterizations. The morphologies of CNTs and CNx were characterized with field emission scanning electron microscopy (SEM, Hitachi S-4800, 5 kV). The structures of CNTs and CNx and the dispersion of Pt on both of them were investigated with transmission electron microscopy (TEM, Philips CM10, 80 kV). High-resolution TEM (HRTEM) images were obtained with a JEOL 2010F microscope, operating at 200 kV. X-ray photoelectron spectroscopy (XPS, Kratos Axis Ultra Al, alpha, 14 kV) was applied for the analysis of nitrogen in the CNx. Raman data were obtained with a Horiba Jobin Yvon high-resolution (HR800) confocal Raman spectrometer, which operates with an incident laser beam at 632.8 nm. Measurements of the carbon K-edge near-edge X-ray absorption fine structure (NEXAFS) of the nanotubes were conducted at the spherical grating monochromator (SGM) beamline of the Canadian Light Source, a 2.9 GEV third generation synchrotron source.

2.4. Electrochemical Characterizations. The electrochemical characterizations were conducted in a thermostatted standard three-compartment electrochemical cell using a ring-disk electrode setup with a bipotentiostat (Model PGSTAT-30, Ecochemie, Brinkman Instruments) and rotation control (Pine Instruments). Pt wire and Ag/AgCl (3 M NaCl) served as the counter and reference electrode, respectively. For convenience, all potentials in this paper are referenced to standard hydrogen electrode (SHE).

The working electrode was prepared as follows. Five milligrams of catalyst (Pt/CNTs or Pt/CNx) were suspended in 1 mL of 2-propanol solution containing 20 μL of a 5 wt % Nafion solution (Ion Power Inc., USA) with ultrasonication to achieve a uniform ink. The catalyst thin film was prepared by casting 20 μL of the ink onto a glassy carbon electrode (5 mm in diameter, Pine Instruments). The electrode was dried at 60 °C for 10 min.

The catalytic activity for the ORR was evaluated with a rotating ring-disk electrode (RRDE, Pine Instruments). Before testing began, the electrode was cycled in Ar saturated 0.5 M H_2SO_4 solution until steady-state cyclic voltammetry was reached. O_2 was then bubbled for 30 min to achieve saturation. With gentle O_2 bubbling, RRDE tests were conducted at 5 mV/s with a rotation speed of 1600 rpm (revolution per minute). The gold ring was set at 1.2 V,[30] where the H_2O_2 formed on the disk during oxygen reduction is readily reoxidized. All of the electrochemical experiments were performed at 25 °C.

2.5. Membrane-Electrode Assemble (MEA) Fabrication and Single Fuel Cell Test. Before the MEA fabrication, the electrolyte membrane (Nafion 112, DuPont Inc., USA) was pretreated according to the following three steps. First, the membrane was cleaned by immersion in a 3% H_2O_2 aqueous solution at 90 °C for 1 h. Second, after rinsing with deionized water, it was boiled in 1 M H_2SO_4 for 1 h. Finally, the membrane was rinsed and boiled in deionized water to remove H_2SO_4 completely.

An ink of the catalysts and Nafion solution (3:1 in weight ratio of catalyst to dry Nafion) in iso-propanol was prepared with ultrasonication and pasted on the gas diffusion electrode (E-TEK Division, PEMEAS Fuel Cell Technologies, Somerset, NJ, USA) at a Pt loading of 0.2 mg/cm^2. Afterward, it was dried in a vacuum oven at 90 °C for 3 h. A Nafion layer was then brushed on the top of the catalysts at 0.6 mg/cm^2. The prepared electrode was dried
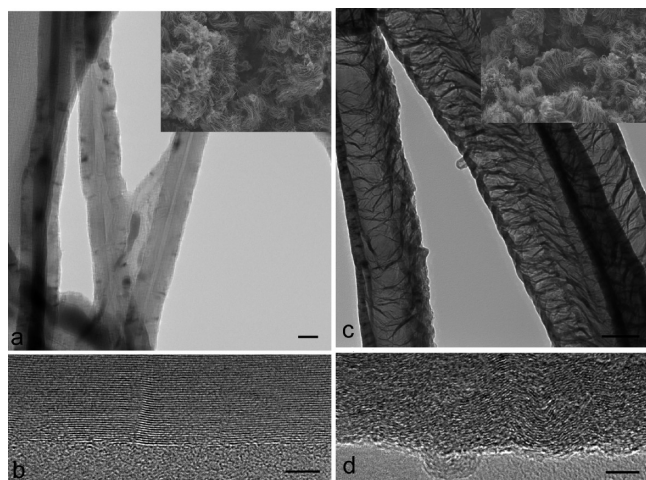
Figure 1. TEM and HRTEM images of CNTs (a and b) and CNx (c and d), inserts: the corresponding SEM images. Scale bars: 20 nm in a; 100 nm in c; 5 nm in c and d.
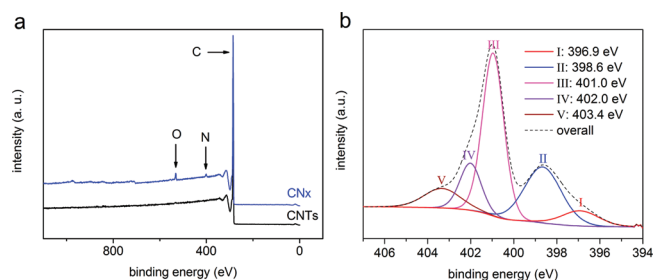

Figure 2. XPS spectra: (a) Survey scan of CNTs and CNx; (b) N 1s of CNx.

in vacuum oven at 90 °C for 1 h and was then ready for MEA fabrication.

With the standard gas diffusion electrode (0.5 mg_{Pt}/cm^2, E-TEK Division, PEMEAS Fuel Cell Technologies, Somerset, NJ, USA) as the anode, the prepared electrode as the cathode, and Nafion 112 as the membrane, the MEA was hot pressed at 135 °C and 150 psi for 2 min.

All of the MEAs were tested at 80 °C, with both H_2 and O_2 at a flow rate of 500 sccm, cathode, and anode back pressure at 25 psig. Prior to the recording of the polarization curves, the MEA was stabilized at 0.6 V for 5 h in order to activate the MEA.

3. RESULTS AND DISCUSSIONS

3.1. Physical Characterizations. Figure 1 shows representative SEM and TEM images of the synthesized CNTs and CNx. From the SEM images (inserts of parts a and c of Figure 1), it can be seen that CNTs and CNx are obtained on the substrate with high density. TEM images illustrate the differences between CNTs and CNx. The morphology of CNTs is a tubular structure with hollow cores (as shown in part a of Figure 1), which differs remarkably from CNx. The CNx structure is divided into hollow sections separated by one to a few graphite layers; that is, CNx shows bamboolike structures with defined compartments or with bridging layers, as presented in part c of Figure 1. The special structure of CNx indicates that nitrogen atoms are successfully incorporated into the graphite matrix,[31] which is confirmed by XPS results discussed later on. Both CNTs and CNx have uniform distributions in tube diameters. The tube diameter of CNTs is about 35−50 nm, whereas CNx shows a much larger diameter, from 120 to 150 nm. More important differences lie on the sidewalls revealed by the HRTEM images in parts b and d of Figure 1. The surface morphology and atomic arrangement of the CNTs are flat and ordered with fine graphite layers respectively, as shown in part b of Figure 1. However, the surface morphology and atomic arrangement of CNx become rough and disordered (part d of Figure 1). The disruptions and irregular curvatures in graphene stacking in CNx are due to the propensity of incorporated nitrogen to form pentagonal and hexagonal defects in the graphene layers. The introduction of such defects disrupts the planar hexagonal arrangement of carbon atoms in CNTs and results in the rough surface of CNx.
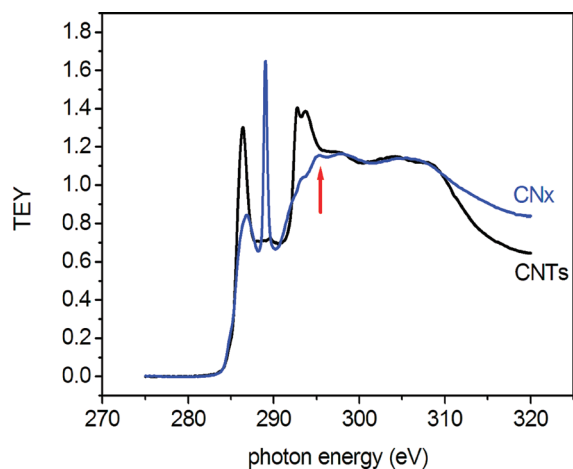
To analyze the elemental composition as well as the chemical-bonding environment of doped nitrogen atoms, XPS measurements were conducted on CNTs and CNx. The XPS survey scans are depicted in part a of Figure 2. Both CNTs and CNx show a strong peak at 285 eV, which can be assigned to C 1s from sp^2 hybridized carbon in the nanotube. Compared with CNTs, CNx exhibits two extra peaks at 532 and 401 eV, which correspond to O 1s and N 1s peaks, respectively. There exhibit many more edge planes on the surface of CNx compared to CNTs. The carbon atoms on the edge plane can be easily oxidized to oxygen-containing functionalities,[32,33] and oxygen molecules can be also physisorbed onto the rough surface. This results in an O 1s peak on the XPS spectrum of CNx. The existence of nitrogen peak confirms the successful incorporation of nitrogen atoms into the graphite matrix. The atomic concentration of N defined as $N/(N + C)$ was estimated by the peak area corrected by the sensitivity factors.[34,35] The nitrogen concentration in the CNx is 8.4 atom %. A fine-scanned N 1s peak (part b of Figure 2) was obtained to elucidate the chemical natures of the nitrogen in CNx. The asymmetric N 1s peak centered at 401 eV can be deconvoluted into five peaks at 396.9, 398.6, 401.0, 402.0, and 403.4 eV from low to high binding energy. They are ascribed as tetrahedral, pyridinic, graphitic, oxidized, and molecular nitrogen, respectively.[28] Tetrahedral nitrogen is bonded to sp^3 C due to an undecomposed N−H bond in the melamine precursor.[36] Pyridinic nitrogen is bonded to two carbon atoms and donates one p electron to the aromatic π system (C−N=C).[37−39] Nitrogen-doping in the pyridinic sites is believed to be responsible for both the wall roughness and the interlinked morphologies.[40] This is in good agreement with the TEM observations above. Graphitic nitrogen is a nitrogen atom, which replaces a carbon atom within a graphite plane and is bonded to three carbon atoms $\left(\begin{smallmatrix} C \\ | \\ C-N-C \end{smallmatrix} \right)$.[37−39] Oxidized nitrogen is oxidized pyridinic nitrogen, which is bonded to two carbon atoms and one oxygen atom $\left(\begin{smallmatrix} O \\ | \\ C-N-C \end{smallmatrix} \right)$.[41−44] Molecular N_2 are nitrogen molecules adsorbed/intercalated at the carbon walls or trapped in the compartments, which has been confirmed by the X-ray absorption near-edge structure analysis[45] and scanning transmission X-ray microscopy.[46] From the peak areas, the doped nitrogen atoms are mainly pyridinic, graphitic, and oxidized nitrogen.

The carbon K-edge near-edge X-ray absorption fine structure (NEXAFS) was measured to compare the structures of CNTs and CNx, as presented in Figure 3. The total electron yield (TEY) is surface sensitive with a typical probing depth of a few nanometers. According to the dipole-transition selection rule, all spectral features are caused by transitions from the C 1s core level to p-like final unoccupied states. The two peaks at 286.5 and 292.8 eV are attributed to the C 1s to unoccupied states of C−C
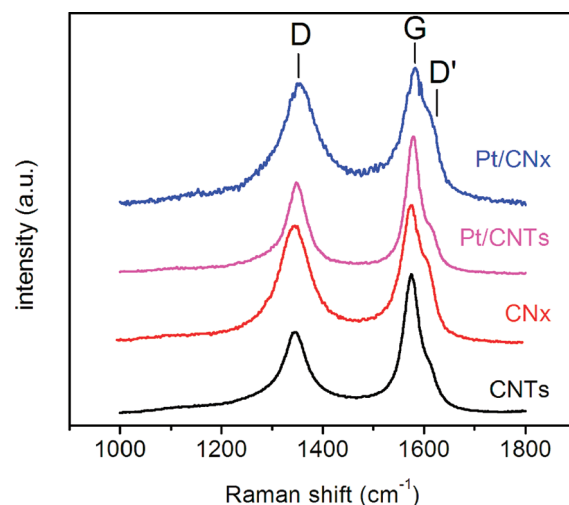
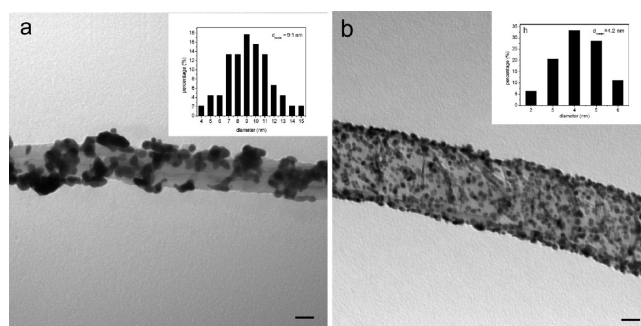**Figure 3.** TEY of carbon K-edge NEXAFS of CNTs and CNx.

Figure 4. Raman spectra of CNTs, CNx, Pt/CNTs, and Pt/CNx (all the spectra are normalized to the G-band intensity).
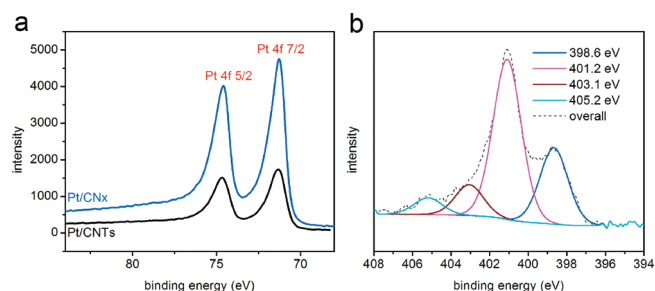

Figure 5. TEM images and size distribution histograms (inserts) of Pt nanoparticles deposited on CNTs (a) and CNx (b), scale bars are in 20 nm.

π^* and C–C σ^*, respectively.[47] The similar features in both spectra indicate a similar graphite structure in both samples. The differences between CNTs and CNx lies in the peak position and profile, and features in the region between the π^* and σ^* resonance. Several features are apparent. First, the π^* is significant broadened and shifted to higher binding energy. This shift and accompanying broadening is due to the incorporation of N in the aromatic (π) system, resulting in a shift to higher energy from the different chemical environment of C not directly bonded to the N. Second, there is a sharp peak at 289.1 eV, which is from defect sites in the graphite structure.[46,47] It is reported that N dopants suppress the formation of sp^2 carbon bonds because of strong bonds between N atoms and the neighboring host C atoms.[48] The much higher intensity of the 289.1 eV peak in CNx implies more defects in CNx. This conclusion is consistent with the HRTEM observations and XPS results and was recently confirmed by STXM observation of an individual CNx.[46] Finally, the spectroscopic features above the graphitic like σ^* resonance exhibits an additional feature at ~296.5 eV (marked with an arrow). This is most likely due to the shape resonance (multiple scattering) arising from the C–N bond.

The structural defectiveness caused by nitrogen doping is further evaluated quantitatively with Raman spectroscopy (Figure 4). The analysis of the peak positions and intensities gives information about the changes of the structural characteristics of the samples, namely graphite layer defectiveness, resulting from nitrogen doping. Both samples exhibit two strong bands near 1348 and 1579 cm^{-1}, corresponding to the D- and G-bands, respectively.[49] The G-band indicates the presence of crystalline graphite carbon, whereas the D-band is attributed to disorders in the graphite structure. The D′-band, which is a shoulder of the G-band at a higher frequency, corresponds to second-order Raman scattering from the variation of the D-band. The ratio of the intensities of the two bands (I_D/I_G) is an indicator of the degree of disorder within the samples.[49] The I_D/I_G ratios for CNTs and CNx are 0.58 and 0.86, respectively. The much higher I_D/I_G ratio and D′-band intensity of CNx implies the higher defectiveness of the graphitelike layers by nitrogen doping. Therefore, Raman results agree well with the above conclusion that CNx contains more defects than CNTs.

To use CNTs and CNx as catalyst supports, Pt nanoparticles were deposited on them. Figure 5 reveals the dispersion of Pt nanoparticles on CNTs and CNx, and the corresponding particle size distribution histograms. On CNTs, the Pt nanoparticles size is distributed from 4 to 15 nm, whereas Pt nanoparticles on CNx show a uniform dispersion from 2 to 6 nm. The mean size of Pt/CNx is 4.2 nm, which is much smaller than that of Pt/CNTs, 9.1 nm (as listed in Table 1). Thus, Pt nanoparticles with a denser population were obtained on CNx, with no evidence of agglomeration. In comparison, Pt nanoparticles aggregated into large clusters on CNTs and some surfaces of CNTs are free of Pt nanoparticle coverage. Because the deposition of Pt nanoparticles on the two supports was conducted under the same conditions, the difference in the dispersion behavior must come from the difference between these two supports. These results suggest that nitrogen doping into CNTs can affect the particle size and distribution of Pt during the reduction of $H_2PtCl_6 \cdot 6H_2O$ by ethylene glycol.

Studies have shown that nitrogen doping not only facilitates the high dispersion of Pt nanoparticles on the carbon surface but also results in a stronger interaction between Pt and the supports.[50] First of all, the presence of the homogeneously distributed nitrogen species on the surfaces of CNx effectively provides nucleation sites and thus promotes a higher dispersion of Pt nanoparticles. Our previous study indicates that Pt prefers to nucleate along the kinks on the CNx surface, where nitrogen atoms are located.[51] Second, there are more disorders on the surface of CNx than CNTs (as demonstrated by HRTEM

**Table 1. Particle Size, Electrochemical Parameters, and Catalytic Performances of Pt/CNTs and Pt/CNx**

catalysts	average size (nm)	ECSA (m^2/gPt)	half-wave potential of ORR (V)	kinetic current density of ORR at 0.9 V (mA)	OCV (V)	current density at 0.8 V (A/cm^2)	maximum power density (w/cm^2)
Pt/CNTs	9.1	26.1	0.812	0.167	0.90	0.144	0.470
Pt/CNx	4.2	41.8	0.844	0.332	0.93	0.230	0.876

Figure 6. XPS spectra of Pt/CNx: Pt 4f (a) and N1s (b).

images, NEXAFS and Raman spectroscopy above). The surface defects induced by N-doping almost certainly increases the interaction between Pt nanoparticles and the surface via Pt—N(O) mediated interaction, immobilizing the Pt nanoparticles. Third, nitrogen doping results in an improvement in hydrophilicity and wettability of CNx.[52] The enhanced access of solvated and charged PtCl$_6^{2-}$ ions to the CNx surface can be associated with the superior dispersion of Pt nanoparticles and the avoidance of agglomeration. It is found that CNx is easier to disperse in the solution during experiments. Finally, the electronic structure of CNx is modified by nitrogen doping. Nitrogen atoms doped into CNTs are most likely to be electron donors[53] and result in chemically active localized areas in CNx with a higher electron density.[54] This increase in reductive sites or high local electron density can be explained by the pyridinic, oxidized, and graphitic nitrogen.[55] Thus, CNx could enhance the reduction of H$_2$PtCl$_6$ and lead to a high dispersion of Pt nanoparticles. All of the above factors including surface nitrogen functionalities, surface disorders, improved hydrophilicity, and modified electronic structure contribute to the good dispersion and immobilization of Pt nanoparticles on the CNx surface.

XPS spectra were collected to further confirm the deposition of Pt on CNTs and CNx. The survey scans of Pt/CNTs and Pt/CNx show the signals of the corresponding elements (Figures S1 and S2 of the Supporting Information). Two distinct sharp Pt (4f 7/2) and Pt (4f 5/2) peaks around 71.00 and 74.34 eV respectively are clearly observed on Pt/CNTs and Pt/CNx (part a of Figure 6). These are typical values for zero-valence Pt, indicating that the deposited Pt is metallic.

The fine-scanned N 1s peak of CNx after Pt deposition was also analyzed in part b of Figure 6. Compared with the chemical components of nitrogen in pristine CNx discussed above, tetrahedral and oxidized nitrogen at 396.9 and 402.0 eV disappear. Pyridinic, graphite and molecular nitrogen at 398.6, 401.2, and 403.1 eV respectively are still observed. A new peak at 405.2 eV appears. This new peak can be ascribed to chemisorbed nitrogen oxides.[44] It seems that the tetrahedral and oxidized nitrogen convert to chemisorbed nitrogen oxides after Pt deposition. However, more work need to be done to elucidate this phenomenon.
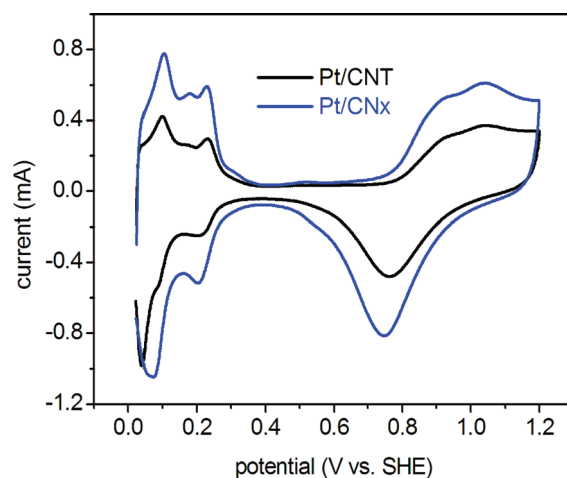
Figure 7. Cyclic voltammograms of Pt/CNTs and Pt/CNx in Ar saturated 0.5 M H$_2$SO$_4$ at 50 mV/s.

The Raman spectra of Pt/CNTs and Pt/CNx were also taken in comparison of the spectra of the original CNTs and CNx (Figure 4). The similar features suggest that the deposition of Pt nanoparticles cause little changes to the CNTs or CNx. However, the D- and D′-band intensities increase with Pt deposition in relative with the G-band intensity. The I_D/I_G ratios of Pt/CNTs and Pt/CNx are 0.67 and 0.89, increasing from 0.58 and 0.86 for CNTs and CNx, respectively. Because of the preferential deposition of Pt on the defective sites on the surface of CNTs or CNx, a selective surface-enhancement effect of the defect-induced Raman signal (D and D′-band) occurs.[56,57]

3.2. Electrochemical Characterizations. To show that the enhanced dispersion of Pt nanoparticles on CNx improves their catalytic activity toward the ORR, electrochemical characterizations were conducted, in comparison with Pt/CNTs. The cyclic voltammograms of both Pt/CNTs and Pt/CNx are presented in Figure 7. Typical CV curves of Pt are obtained, with H$_2$ adsorption/desorption regions and Pt oxidation/reduction peaks. The electrochemical surface area (ECSA) of Pt is calculated from the charges of H$_2$ adsorption/desorption peaks, assuming a surface density of 1.3×10^{15} atom/cm^2 for polycrystalline Pt.[11] Pt/CNx shows a larger ECSA of 41.8 m^2/g$_{Pt}$ compared to that of Pt/CNTs, whose ECSA is 26.1 m^2/g$_{Pt}$ (as listed in Table 1). Higher ECSA of Pt/CNx than Pt/CNTs must originate from the higher dispersion of Pt nanoparticles and smaller Pt particle size. It will be responsible for the better electrochemical catalytic activity discussed below.

Figure 8 shows The RRDE tests for ORR on the Pt/CNTs and Pt/CNx under the same experimental conditions. From Figure 8, the kinetic current density reaches a plateau at low potential, which implies that ORR is diffusion-controlled. At high potential region, the ORR is under mixed diffusion-kinetic control. The half-wave potential, an indicator of activity toward ORR, of

3773

dx.doi.org/10.1021/jp108864y |*J. Phys. Chem. C* 2011, 115, 3769–3776
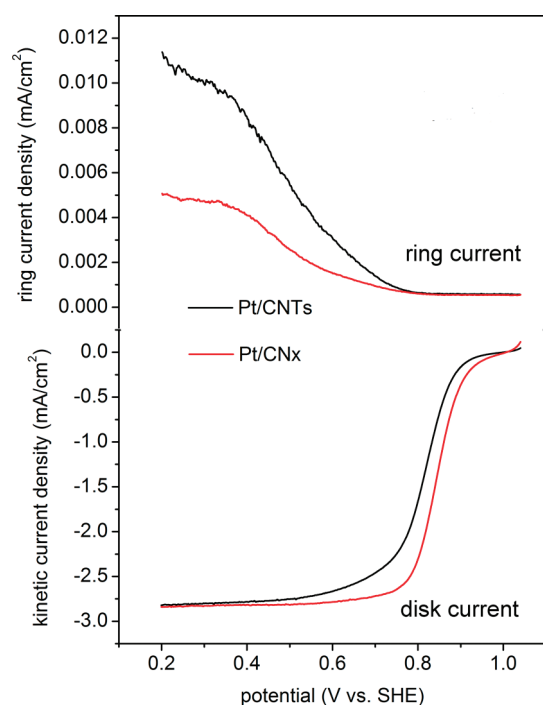
Figure 8. RRDE tests toward ORR on Pt/CNTs and Pt/CNx in the cathodic sweep at 1600 rpm in O_2 saturated 0.5 M H_2SO_4 at 5 mV/s and 25 °C.

Pt/CNx shifts positively by 32 mV, compared with Pt/CNTs as listed in Table 1. Thus, nitrogen doping on the supports enhances the electrocatalytic activity of the deposited Pt toward ORR. The substantial enhancement for ORR can be obviously credited to the larger ECSA as demonstrated above. The ECSA of Pt/CNx is 1.60 times of that of Pt/CNTs, as listed in Table 1. At 0.9 V, the kinetic current density of Pt/CNx is 0.332 mA, whereas that of Pt/CNTs is 0.167 mA. That is, the kinetic current (at 0.9 V) of Pt/CNx is 1.99 times higher than that of Pt/CNTs. The specific activity, defined by kinetic current at 0.9 V divided by ECSA, of Pt/CNx is 1.34 times of Pt/CNTs. Therefore, nitrogen doping not only increases the ECSA, but also improves the intrinsic electrocatalytic activity toward ORR.

It is well-known that the ORR can proceed by two pathways, (i) a two-electron reduction to H_2O_2 (R1), and (ii) a four-electron reduction to H_2O (R2). The ring current

$$O_2 + 2H^+ + 2e^- \rightarrow H_2O_2 \tag{1}$$

$$O_2 + 4H^+ + 4e^- \rightarrow 2H_2O \tag{2}$$
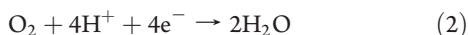
density (Figure 8), at 1.2 V, corresponds to the fraction of H_2O_2 during ORR. Compared with the disk current density, the ring current density is negligible, which indicates that the ORR mainly goes through a four-electron pathway. The ring current density of Pt/CNx is smaller than that of Pt/CNTs, which means that Pt/CNx favors a four-electron pathway more than the Pt/CNTs. It is well recognized that H_2O_2 accelerates the degradation of the Nafion electrolyte membrane in the PEMFC.[2] Hence, a reduced production of H_2O_2 in Pt/CNx can increase the durability of PEMFCs. This is another benefit with CNx as the Pt supports.

It has been shown that CNx itself can act as an electrocatalyst for ORR.[19,20] As shown in Figure S3 in Supporting Information, CNx shows a higher activity for ORR than CNTs. However, the
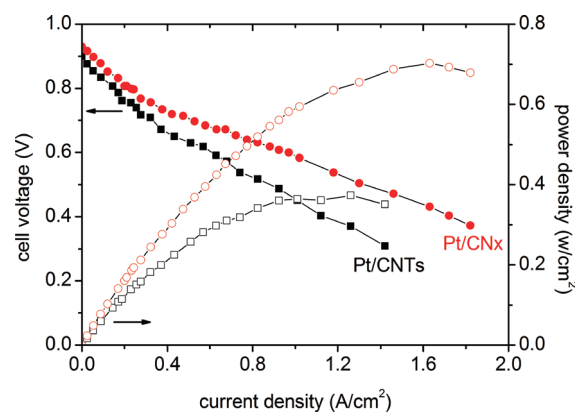
Figure 9. Comparison of single fuel cell performances with Pt/CNTs and Pt/CNx as the cathode catalysts at a Pt loading of 0.2 mg/cm^2. Commercial gas diffusion electrode (0.5 mg$_{Pt}$/cm^2, E-TEK) as the anode; H_2/O_2 at 80 °C; Nafion 112 membrane; 25/25 psig anode and cathode back pressure respectively.

contributions from the support materials count for little in comparison with the Pt catalysts. The improved activity of Pt/CNx can be also ascribed to the specific interaction between CNx and the overlying Pt catalysts.[58] This interaction can result in modifications to the electronic structure of the overlying Pt nanoparticles which in turn changes their catalytic activity.[50] CNx is most likely to be an electron donor. When deposited with Pt, the electron transfer from the CNx support to the unfilled orbitals of Pt could occur via the nitrogen group. This process would lead to the higher electron density of Pt nanoparticles, keep a clean metallic surface, and thus enhance the electrocatalytic activity. The Pt 4f peak shift in XPS,[59] first principle calculations on binding energy between Pt and CNx,[25,26] and our previous durability study of Pt/CNx[27] all indicate a strong metal−support interaction between CNx and the overlying Pt nanoparticles.

3.3. Fuel Cell Performances. The H_2/O_2 fuel cell performances of Pt/CNTs and Pt/CNx as the cathode catalysts are shown in Figure 9. Pt/CNx showed a better performance than Pt/CNTs. The comparison of the performances is listed in Table 1. Pt/CNx exhibited an open circuit voltage (OCV) of 0.93 V, which is higher than 0.9 V of Pt/CNTs. At the cell voltage of 0.8 V, Pt/CNTs have a current density of 0.144 A/cm^2, whereas Pt/CNx is 0.230 A/cm^2, with an improvement of 59.7%. Furthermore, the maximum power density of Pt/CNx is 0.876 W/cm^2, which is larger than 0.470 W/cm^2 of Pt/CNTs. Because the same anode catalyst and membrane were used in the tests and the cathode dominates the fuel cell performance, it can be concluded that Pt/CNx is a better cathode catalyst than Pt/CNTs. That is, CNx is superior to CNTs as the Pt supports. The results are in good agreement with the RRDE tests above. And, the mechanism for the enhancement in fuel cell performance can be explained in the same way as above.

4. CONCLUSIONS

CNTs and CNx have been synthesized with the FCCVD method under similar conditions for a comparative test. The structure of CNx is changed considerably by the doping of nitrogen into the graphene matrix. XPS, NEXAFS and Raman characterizations reveal the structural differences between CNTs and CNx in details. With the ethylene glycol reduction method, Pt

nanoparticles have been deposited on these two supports. Pt/CNx shows a more uniform dispersion with smaller particle size than Pt/CNTs. Pt/CNx exhibits higher catalytic activity toward ORR than Pt/CNTs, as indicated by a larger kinetic current, higher half-wave potential, and higher four-electron transfer efficiency to H_2O. Pt/CNx, as a cathode catalyst, also shows higher fuel cell performance in a single cell test than that of Pt/CNTs.

■ ASSOCIATED CONTENT

ⓢ Supporting Information. XPS survey scans of Pt/CNTs and Pt/CNTs; ORR activities of CNTs, CNx, Pt/CNTs, and Pt/CNx. This material is available free of charge via the Internet at http://pubs.acs.org.

■ AUTHOR INFORMATION

Corresponding Author
*E-mail: xsun@eng.uwo.ca. Tel: +1-519-6612111, Ext. 87759. Fax: +1-519-6613020.

■ ACKNOWLEDGMENT

■ REFERENCES

(1) Larminie, J.; Dicks, A. *Fuel Cell Systems Explained*, 2nd ed.; West Sussex, England: John Wiley & Sons Ltd., 2003.

(2) Borup, R.; Meyers, J.; Pivovar, Br.; Kim, Y. S.; Mukundan, R.; Garland, N.; Myers, D.; Wilson, M.; Garzon, F.; Wood, D.; Zelenay, P.; More, K.; Stroh, K.; Zawodzinski, T.; Boncella, J.; McGrath, J. E.; Inaba, M.; Miyatake, K.; Hori, M.; Ota, K.; Ogumi, Z.; Miyata, S.; Nishikata, A.; Siroma, Z.; Uchimoto, Y.; Yasuda, K.; kimijima, K.; Iwashita, N. *Chem. Rev.* **2007**, *107*, 3904.

(3) Gasteiger, H. A.; Kocha, S. S.; Sompalli, B.; Wagner, F. T. *Appl. Catal., B* **2005**, *56*, 9.

(4) Yu, X.; Ye, S. *J. Power Sources* **2007**, *172*, 145.

(5) Thompson, S. D.; Jordan, L. R.; Forsyth, M. *Electrochim. Acta* **2001**, *46*, 1657.

(6) Kinoshita, K. *Carbon: Electrochemical and Physicochemical Properties*; New York: John Wiley & Sons, 1988.

(7) Roen, L. M.; Paik, C. H.; Jarvi, T. D. *Electrochem. Solid-State Lett.* **2004**, *7*, A19.

(8) Shao, Y.; Wang, J.; Kou, R.; Engelhard, M.; Liu, J.; Wang, Y.; Lin, Y. *Electrochim. Acta* **2009**, *54*, 3109.

(9) Li, L.; Xing, Y. *J. Electrochem. Soc.* **2006**, *153*, A1823.

(10) Wang, X.; Li, W.; Chen, Z.; Waje, M.; Yan, Y. *J. Power Sources* **2006**, *158*, 154.

(11) Saha, M. S.; Li, R.; Sun, X. *J. Power Sources* **2008**, *177*, 314.

(12) Wang, X.; Waje, M.; Yan, Y. *Electrochem. Solid-State Lett.* **2005**, *8*, A42.

(13) Zhang, S.; Shao, Y.; Yin, G.; Lin, Y. *J. Mater. Chem.* **2010**, *20*, 2826.

(14) Wang, S.; Jiang, S. P.; Wang, X. *Nanotechnology* **2008**, *19*, 265601.

(15) Yang, J.; Goenaga, G.; Call, A.; Liuz, D. *Electrochem. Solid-State Lett.* **2010**, *13*, B55.

(16) Shao, Y.; Yin, G.; Gao, Y.; Shi, P. *J. Electrochem. Soc.* **2006**, *153*, A1093.

(17) Lee, K.; Zhang, J.; Wang, H.; Wilkinson, D. P. *J. Appl. Electrochem.* **2006**, *36*, 507.

(18) Zamudio, A.; Elias, A. L.; Rodriguez-Manzo, J. A.; Lopez-Urias, F.; Rodriguez-Gattorno, G.; Lupo, F.; Ruhle, M.; Smith, D. J.; Terrones, H.; Diaz, D.; Terrones, M. *Small* **2006**, *2*, 346.

(19) Lefevre, M.; Proietti, E.; Jaouen, F.; Dodelet, J. *Science* **2009**, *324*, 71.

(20) Bezerra, C. W.; Zhang, L.; Lee, K.; Liu, H.; Marques, A. L.; Marques, E.; Wang, H.; Zhang, J. *Electrochim. Acta* **2008**, *50*, 4937.

(21) Saha, M. S.; Li, R.; Sun, X.; Ye, S. *Electrochem. Commun.* **2009**, *11*, 438.

(22) Yue, B.; Ma, Y.; Tao, H.; Yu, L.; Jian, G.; Wang, X.; Wang, X.; Lu, Y.; Hu, Z. *J. Mater. Chem.* **2008**, *18*, 1747.

(23) Choi, B.; Yoon, H.; Park, I.; Jang, J.; Sung, Y. *Carbon* **2007**, *45*, 2496.

(24) Sun, C.; Chen, L.; Su, M.; Hong, L.; Chyan, O.; Hsu, C.; Chen, K.; Chang, T.; Chang, L. *Chem. Mater.* **2005**, *17*, 3749.

(25) Li, Y.; Hung, T.; Chen, C. *Carbon* **2009**, *47*, 850.

(26) An, W.; Turner, C. H. *J. Phys. Chem. C* **2009**, *113*, 7069.

(27) Chen, Y.; Wang, J.; Liu, H.; Li, R.; Sun, X.; Ye, S.; Knights, S. *Electrochem. Commun.* **2009**, *11*, 2071.

(28) Liu, H.; Zhang, Y.; Li, R.; Sun, X.; Désilets, S.; Abou-Rachid, H.; Jaidann, M.; Lussier, L. *Carbon* **2010**, *48*, 1498.

(29) Bock, C.; Paquet, C.; Couillard, M.; Botton, G. A.; MacDougall, B. R. *J. Am. Chem. Soc.* **2004**, *126*, 8028.

(30) Murthi, V. S.; Urian, R. C.; Mukerjee, S. *J. Phys. Chem. B* **2004**, *108*, 11011.

(31) Wang, E. G. *J. Mater. Res.* **2006**, *21*, 2767.

(32) Jianga, W.; Nadeaub, G.; Zaghib, K.; Kinoshita, K. *Thermochim. Acta* **2000**, *351*, 85.

(33) Shalagina, A. E.; Ismagilov, Z. R.; Podyacheva, O. Yu.; Kvon, R. I.; Ushakov, V. A. *Carbon* **2007**, *45*, 1808.

(34) Nath, M.; Satishkumar, B. C.; Govindaraj, A.; Vinod, C. P.; Rao, C. *Chem. Phys. Lett.* **2000**, *322*, 333.

(35) Kim, S. Y.; Lee, J.; Na, C. W.; Park, J.; Seo, K.; Kim, B. *Chem. Phys. Lett.* **2005**, *413*, 300.

(36) Ghosh, K.; Kumar, M.; Maruyama, T.; Ando, Y. *Carbon* **2009**, *47*, 1565.

(37) Tao, X. Y.; Zhang, X. B.; Sun, F. Y.; Cheng, J. P.; Liu, F.; Luo, Z. Q. *Diamond Relat. Mater.* **2007**, *16*, 425.

(38) Zhang, G. Y.; Ma, X. C.; Zhong, D. Y.; Wang, E. G. *J. Appl. Phys.* **2002**, *91*, 9324.

(39) Morant, C.; Andrey, J.; Prieto, P.; Mendiola, D.; Sanz, J. M.; Elizalde, E. *Phys. Status Solidi A* **2006**, *203*, 1069.

(40) Liu, J.; Webster, S.; Carroll, D. L. *J. Phys. Chem. B* **2005**, *109*, 15769.

(41) Matter, P. H.; Zhang, L.; Ozkan, U. S. *J. Catal.* **2006**, *239*, 83.

(42) Pels, J. R.; Kapteijn, F.; Moulijn, J. A.; Zhu, Q.; Thomas, K. M. *Carbon* **1995**, *33*, 1641.

(43) Casanovas, J.; Ricart, J. M.; Rubio, J.; Illas, F.; Jimenez-Meteos, J. M. *J. Am. Chem. Soc.* **1996**, *118*, 8071.

(44) Biniak, S.; Szymanski, G.; Siedlewski, J.; Swiatkowsky, A. *Carbon* **1997**, *35*, 1799.

(45) Choi, H. C.; Bae, S. Y.; Jang, W.; Park, J.; Song, H. J.; Shin, H.; Jung, H.; Ahn, J. *J. Phys. Chem. B* **2005**, *109*, 1683.

(46) Zhou, J.; Wang, J.; Liu, H.; Banis, M. N.; Sun, X.; Sham, T. *J. Phys. Chem. Lett.* **2010**, *1*, 1709.

(47) Tang, Y. H.; Sham, T. K.; Hu, Y. F.; Lee, C. S.; Lee, S. T. *Chem. Phys. Lett.* **2002**, *366*, 636.

(48) Pong, W. F.; Yueh, C. L.; Chang, Y. D.; Tsai, M. H.; Chang, Y. K.; Chen, Y. Y.; Lee, J. F.; Wei, S. L.; Wen, C. Y.; Chen, L. C.; Chen, K. H.; Ling, I. N.; Chengh, H. F. *J. Synchrotron Rad.* **2001**, *8*, 145.

(49) Chuang, C. C.; Huang, J. H.; Chen, W. J.; Lee, C. C.; Chang, Y. Y. *Diamond Relat. Mater.* **2004**, *13*, 1012.

(50) Shao, Y.; Sui, J.; Yin, G.; Gao, Y. *Appl. Catal. A: Environmental* **2008**, *79*, 89.

(51) Sun, S.; Zhang, G.; Zhong, Y.; Liu, H.; Li, R.; Zhou, X.; Sun, X. *Chem. Commun.* **2009**, 7048.

(52) Zhou, Y.; Pasquarelli, R.; Holme, T.; Berry, J.; Ginleyc, D.; O'Hayre, R. *J. Mater. Chem.* **2009**, *19*, 7830.

(53) Strelko, V. V.; Kuts, V. S.; Throwerb, P. A. *Carbon* **2000**, *38*, 1499.

(54) Nevidomskyy, A. H.; Csányi, G.; Payne, M. C. *Phys. Rev. Lett.* **2003**, *91*, 105502.

(55) Biniak, S.; Szymanski, G.; Siedlewski, J.; Swiatkowski, A. *Carbon* **1997**, *35*, 1799.

(56) Lin, Y.; Watson, K. A.; Fallbach, M. J.; Ghose, S.; Smith, J. G.; Delozier, D. M.; Cao, W.; Crooks, R. E.; Connell, J. W. *ACS Nano* **2009**, *3*, 871.

(57) Hao, Q.; Juluri, B. K.; Zheng, Y. B.; Wang, B.; Chiang, I.; Jensen, L.; Crespi, V.; Eklund, P. C.; Huang, T. J. *J. Phys. Chem. C* **2010**, *114*, 18059.

(58) Ye, S.; Vijh, A. K.; Dao, L. H. *J. Electrochem. Soc.* **1997**, *144*, 90.

(59) Lei, Z.; An, L.; Dang, L.; Zhao, M.; Shi, J.; Bai, S.; Cao, Y. *Microporous Mesoporous Mater.* **2009**, *119*, 30.